AGU PUBLICATIONS

JGR

Journal of Geophysical Research: Space Physics

RESEARCH ARTICLE
10.1002/2015JA021506

Special Section:
Low-Frequency Waves in Space Plasmas

MESSENGER survey of in situ low frequency wave storms between 0.3 and 0.7 AU

S. A. Boardsen[1,2], L. K. Jian[2,3], J. L. Raines[4], D. J. Gershman[3,5], T. H. Zurbuchen[4], D. A. Roberts[2], and H. Korth[6]

[1]Goddard Planetary Heliophysics Institute, University of Maryland, Baltimore County, Baltimore, Maryland, USA, [2]Heliophysics Science Division, NASA Goddard Space Flight Center, Greenbelt, Maryland, USA, [3]Goddard Planetary Heliophysics Institute, University of Maryland, College Park, Maryland, USA, [4]Department of Climate and Space Sciences and Engineering, University of Michigan, Ann Arbor, Michigan, USA, [5]Geospace Physics Laboratory, NASA Goddard Space Flight Center, Greenbelt, Maryland, USA, [6]Johns Hopkins University Applied Physics Laboratory, Laurel, Maryland, USA

Key Points:
- MESSENGER observations of low-frequency storms are surveyed between 0.3 and 0.7 AU
- The occurrence rate of these storms is about 6 times larger than that of previous studies
- The radial power variation of the right handed storms is not consistent with a source near the Sun

Correspondence to:
S. A. Boardsen,
scott.a.boardsen@nasa.gov

Citation:
Boardsen, S. A., L. K. Jian, J. L. Raines, D. Gershman, T. H. Zurbuchen, D. A. Roberts, and H. Korth (2015), MESSENGER survey of in situ low frequency wave storms between 0.3 and 0.7 AU, *J. Geophys. Res. Space Physics*, *120*, 10,207–10,220, doi:10.1002/2015JA021506.

Received 29 MAY 2015
Accepted 16 NOV 2015
Accepted article online 19 NOV 2015
Published online 16 DEC 2015

Abstract MErcury Surface, Space ENvironment, GEochemistry, and Ranging (MESSENGER) magnetometer data was surveyed between 0.3 and 0.7 AU from 6 June 2007 to 23 March 2011 for low-frequency wave (LFW) storms, when the magnetometer was sampling at a rate of at least 2 s^{-1}. A total of 12,197 LFW events were identified, of which 5506 lasted 10 min or longer. The events have a high degree of polarization, are circularly polarized, with wave vectors nearly aligned or antialigned with the interplanetary magnetic field (IMF) at frequencies in the vicinity of the proton cyclotron frequency. These events are observed about 6% of the time, preferentially associated with radially directed inward or outward IMF. Their occurrence rate and median duration do not change much with R, where R is the heliocentric radial distance. For a narrow-frequency window in the solar wind frame, left-handed storms in the spacecraft frame have a power drop off that is roughly proportional to R^{-3} which is consistent with a source close the Sun, while right-handed storms have a power drop off roughly proportional R^{-1} which is not consistent with a source close to the Sun. The power in the left-handed LFW storms is on average greater than the right-handed ones by a factor of 3. In the solar wind frame, the wave frequency decreases from 0.13 to 0.04 Hz moving from 0.3 to 0.7 AU, but the frequency normalized by the local proton cyclotron frequency does not change much with the running median varying from 0.35 to 0.5. The normalized frequency band widths of the wave power spectra increase slightly with R, possibly associated with energy dissipation.

1. Introduction

Coherent low-frequency waves (LFWs) near the proton cyclotron frequency whose wave magnetic field is nearly transverse to the interplanetary magnetic field (IMF) direction are found sporadically in the solar wind. These waves could play an important role in energizing the corona/solar wind ions and in modifying their temperature anisotropy [e.g., *Ofman et al.*, 2001, 2002; *Gary et al.*, 2003; *Podesta and Gary*, 2011a; *Omidi et al.*, 2014a, 2014b]. Studies of these waves have been made at around 0.3 AU [*Jian et al.*, 2010] and at 1 AU [*Tsurutani et al.*, 1994; *Jian et al.*, 2009, 2014; *He et al.*, 2011]. These waves have been observed over the high-latitude Southern and Northern Hemispheres of the Sun between 1.5 and 3.0 AU by the Ulysses spacecraft [*Podesta and Gary*, 2011a]. Between 4.6 to 5.4 AU and heliographic latitudes of −1 to 40°, 34 events over a 640 day interval were identified using the magnetometer on the Ulysses spacecraft [*Murphy et al.*, 1995]. Because the spectral peak in the spacecraft frame in *Murphy et al.* [1995] has a lower cutoff at the local proton cyclotron frequency, these events are attributed to being generated by pickup of interstellar H. In this paper we analyze 4 years of MErcury Surface, Space ENvironment, GEochemistry, and Ranging (MESSENGER) spacecraft cruise phase measurements searching for these waves, covering the period from 6 June 2007 to 23 March 2011, spanning heliocentric radial distances of 0.3 to 0.7 AU.

In the spacecraft frame of reference, these waves are nearly circularly polarized and can be either left or right handed about the IMF direction. At 1 AU, *Jian et al.* [2014] investigated various wave modes that might explain the observations and concluded that they are likely ion cyclotron waves (ICWs) generated in solar wind frame of reference by temperature anisotropy of the ions. They concluded that other sources are unlikely: like interstellar pickup ions He^+ or Ne^+, cometary pickup ions, and solar energetic particles associated with solar flares or interplanetary coronal mass ejections.

These waves are observed when the IMF is preferentially in the radial direction [e.g., *Murphy et al.*, 1995; *Jian et al.*, 2009, 2010, 2014]. The observed angle between the wave vector (k) and the IMF is typically less than 20°

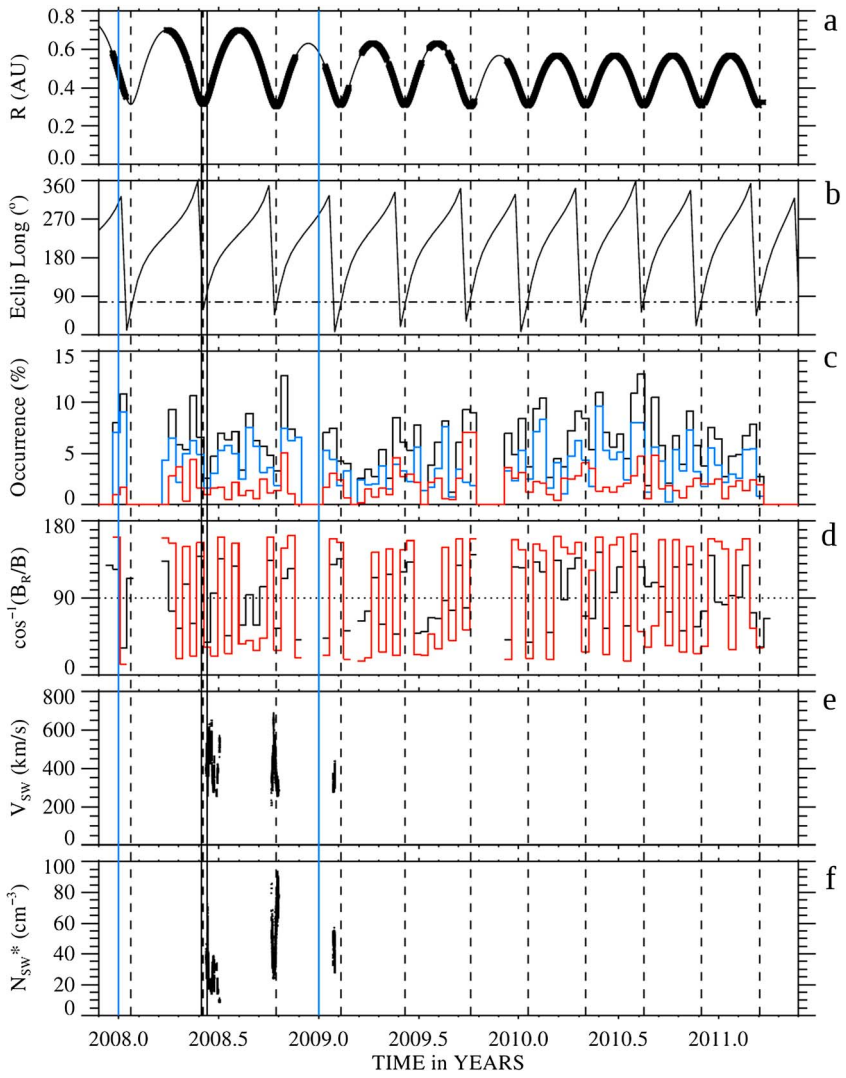

Figure 1. MESSENGER orbit during the cruise phase, orbit insertion was on day 83 of 2011. (a) The thick segments indicate when the magnetometer sampling rate was at least 2 s^{-1}; (b) the ecliptic longitude, the dash-dotted line is the longitude of the focusing cone of interstellar He^{+}; (c) the occurrence probability of LFW storms, black for all storms, red for right-handed storms, blue for left-handed storms; (d) median angle of $\varphi_{BR} = \cos^{-1}(B_R/B)$, black is coverage, red are storms; (e) the solar wind speed when detected by FIPS, and (f) the pseudosolar wind density assigned to the speed measurement (see Figure 5a). The black vertical bars cover the *Jian et al.* [2010] study using MESSENGER near 0.3 AU, and the blue vertical bars cover the *Jian et al.* [2014] at 1 AU.

[e.g., *Jian et al.*, 2009, 2010, 2014], being either nearly field aligned or antifield aligned with the IMF direction. For ICWs generated in the solar wind frame, in which they are left-handed circularly polarized, the Doppler shift relative to the spacecraft frame will be large, because $V_{SW}/V_A > 4$ (where V_{SW} is the solar wind speed and V_A is the Alfvén speed and is a proxy for the ICW phase speed). For wave vectors pointing toward the Sun, they will appear as right-handed circularly polarized waves in the spacecraft frame.

At 0.3 AU, 72% of the wave events in the study of *Jian et al.* [2010] were left handed, and the median wave frequency was 20% higher for the left-handed waves compared to the right-handed waves. At 1.0 AU, 55% of the wave events in the study of *Jian et al.* [2010] were left handed. In this study they found that the power in the left-handed events was usually larger than that of the right-handed events. *Podesta and Gary* [2011b] have shown that when the solar wind proton perpendicular to parallel temperature ratio is >1 and a differential flow velocity $V_{He++} - V_{H+}$ exists between solar wind He^{++} and H^{+} ions, ICWs are generated with a peak growth whose wave vector direction is in the direction given by the difference of $V_{He++} - V_{H+}$, where V_{He++} is

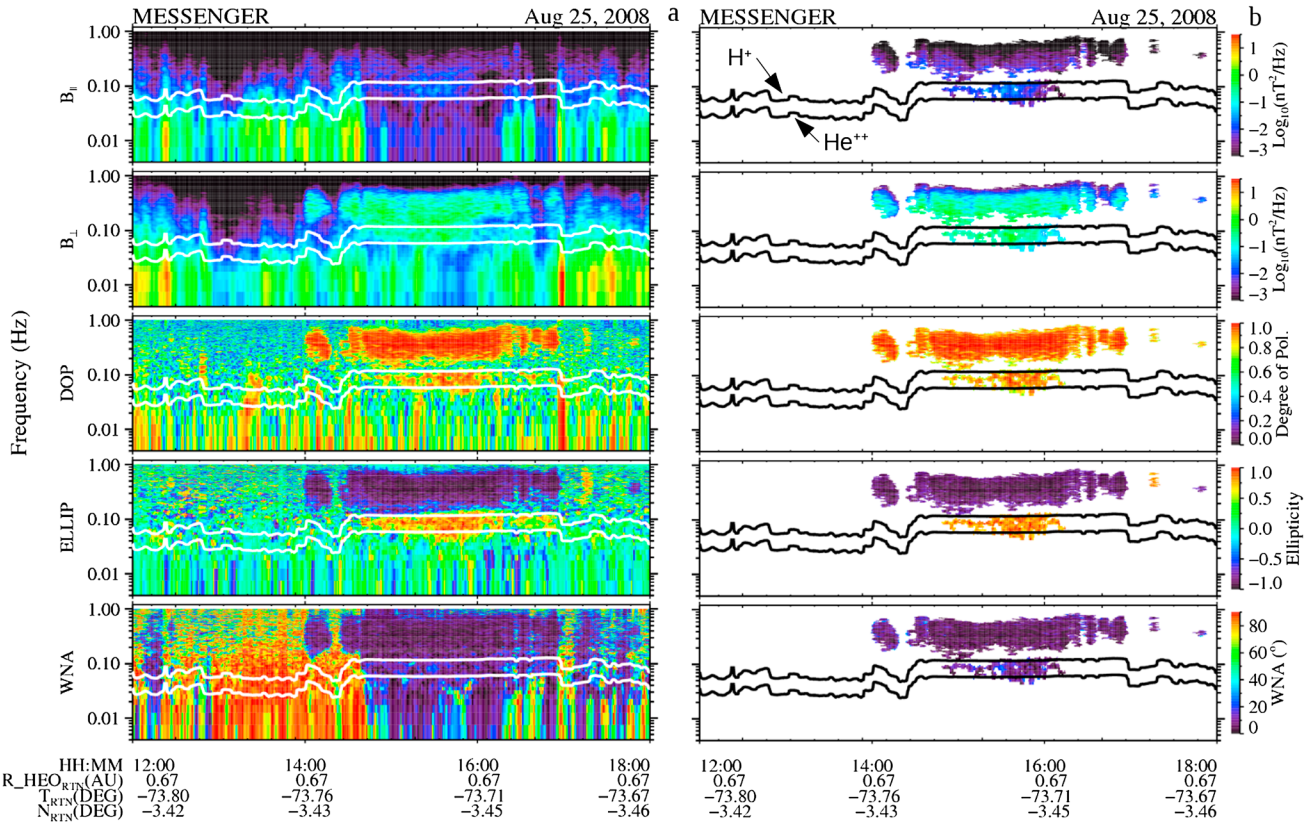

Figure 2. Each panel from top to bottom is a frequency versus time spectrogram of the (top) parallel and (2nd) the perpendicular magnetic power spectral density, (3rd) the degree of polarization (DOP), (4th) the ellipticity (ELLIP), and (bottom) the wave normal angle (WNA).

the He^{++} flow velocity and V_{H+} is the H^+ flow velocity. In general, $|V_{He++}| > |V_{H+}|$ and nearly aligned with the IMF direction [e.g., *Kasper et al.*, 2008], but not always [*Steinberg et al.*, 1996], so k tends to be directed outward.

The study of *Jian et al.* [2010] covered 10 days of MESSENGER magnetometer measurements in 2008, and 1 week of Helios-1 magnetometer measurements in 1976. *Jian et al.* [2014] covered 1 year of STEREO A measurements and were focused on LFW storms which lasted at least 10 min. In that study they found that the intrinsic properties of the wave events were independent of the temporal duration of the events. Herein, we survey the LFW storm occurrence between 0.3 and 0.7 AU partly filling the gap between 0.3 and 1 AU.

2. Data Analysis

The fluxgate magnetometer [*Anderson et al.*, 2007] on the MESSENGER spacecraft makes vector field measurements at a sampling rate of either 1, 2, or 20 s^{-1}. During cruise phase before 2008 the rate was typically at 1 s^{-1}, while after 2008 the rate was typically at 2 s^{-1}. Figure 1a shows the heliocentric distance versus time from day 69 of 2007 to day 83 of 2011 (just before orbital insertion at Mercury). The thick line segments indicate when the sampling rate was at least 2 s^{-1}. These intervals are used in this study and also used to compute coverage parameters for the normalization of occurrence. To resolve the proton cyclotron frequency, we require that the sampling rate was at least 2 s^{-1}. Periods when the sampling rate was 20 s^{-1} were resampled at 2 s^{-1}. Figure 1b is the ecliptic longitude of the spacecraft. The line at 76° indicates the focusing cone of interstellar pickup He^+ [e.g., *Gershman et al.*, 2013]. Figure 1c is the occurrence probability of left handed (blue), right handed (red), and all the storms (black) whose identification is described below, the bin size is 1/30th of a year. The occurrence probability is normalized by data coverage. Figure 1d shows the median angle between IMF direction and the radial direction (φ_{BR}) for coverage (black) and storm observations

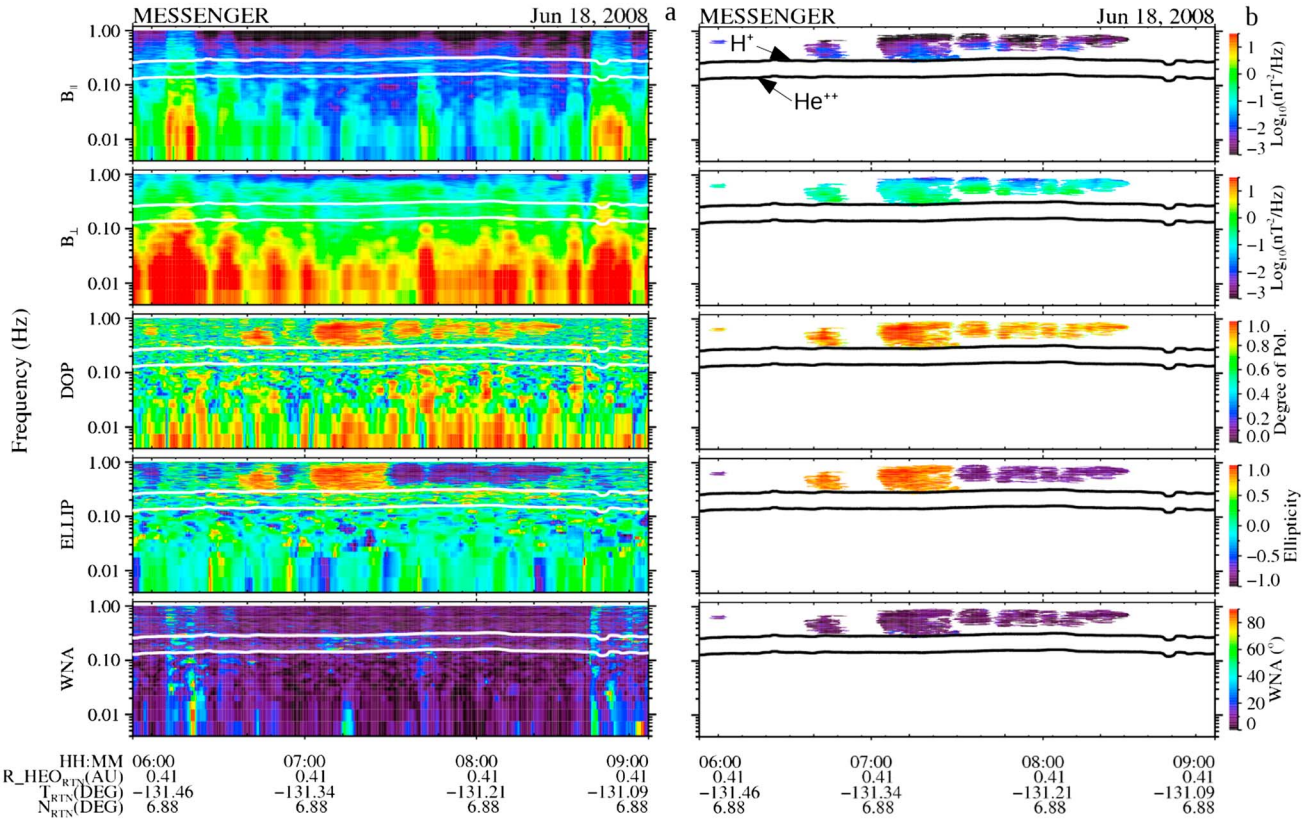

Figure 3. Format is the same as Figure 2 but from a different event, where right- and left-handed events occurred within 1 h of each other.

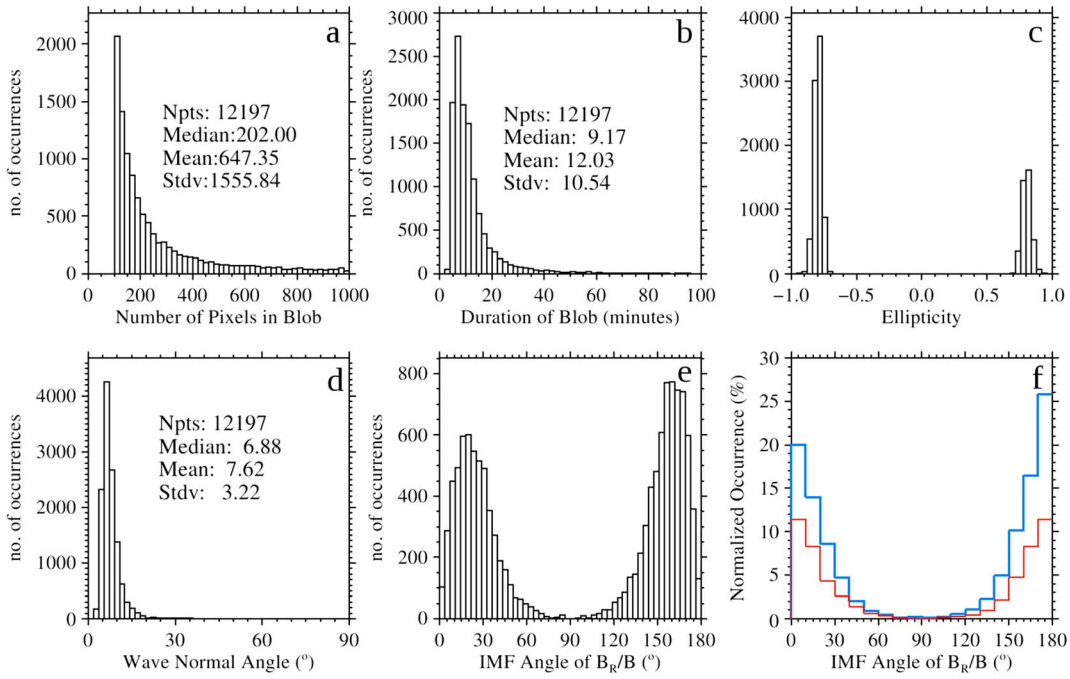

Figure 4. Statistics of the LFW storms (a) number of pixels in the blob, (b) duration in minutes, (c) ellipticity, (d) wave normal angle, (e) the angle given by $\varphi_{BR} = \cos^{-1}(|B_R|/B)$ between the radial direction and the IMF, and (f) the occurrence of the angle between the radial direction and the IMF normalized by coverage, blue is left-handed storms, red is right-handed storms. In the legends: Npts is the number of blobs, and Stdv is the standard deviation.

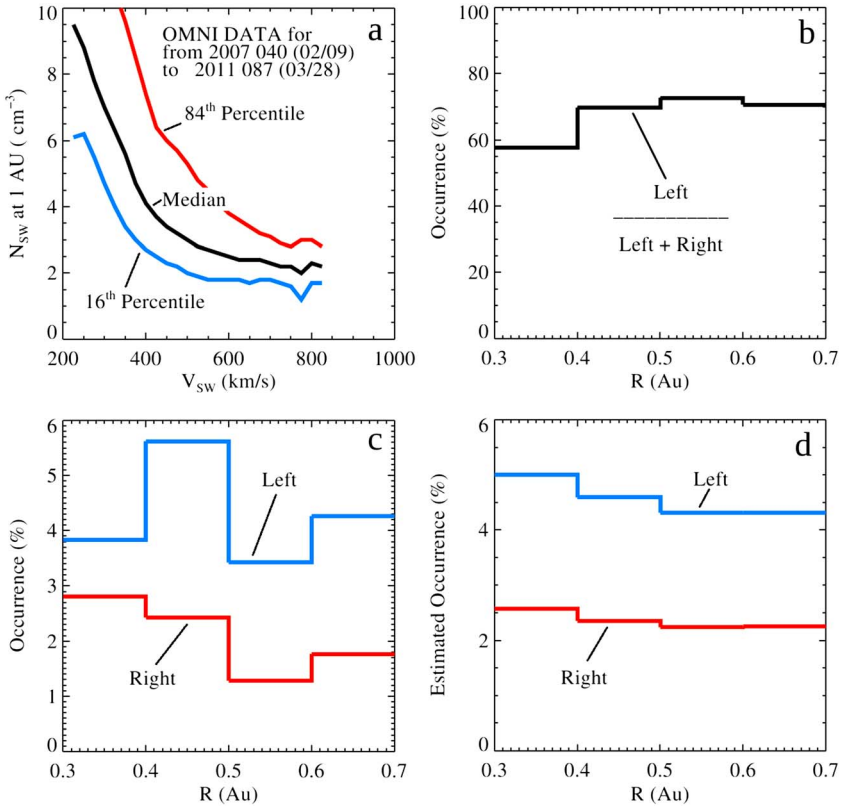

Figure 5. (a) The median density versus median solar wind speed at 1 AU. This relationship is used to assign densities (scaled by R^{-2}) to the FIPS solar wind speed measurements shown in Figure 1e. (b) The ratio of left handed to total storms versus R. (c) Percent occurrence rate per radial bin for left-handed (blue) and right-handed (red) waves in the spacecraft frame. (d) Estimated occurrence probability from the observed $\varphi_{BR} = \cos^{-1}(|B_R|/B)$ in the IMF background and using the probability curves in Figure 4f. In Figures 5b–5d, the radial bin size is 0.1 AU.

(red), where $\varphi_{BR} = \cos^{-1}(B_R/B)$. Figure 1e shows periods when the solar wind is observed by the plasma instrument (not all perihelion intervals have been analyzed for solar wind). Figure 1f shows estimates of the solar wind density from the observed solar wind speed, which is described later.

Throughout this time period, except for periods within ±24 h of planetary flybys, Fast Fourier transforms were made on 200 s time intervals (0.005 Hz frequency (f) resolution) forming power spectral matrices. This analysis covered the entire time period, each time interval is staggered by 25 s from the preceding time interval so they overlap. At each time step the averaged power spectral matrix was formed by averaging that matrix with itself and the spectral matrices of its 2 nearest frequency and its ±3 nearest neighbors in time. Polarization analysis was performed on the averaged power spectral matrix using the method called technique 2 in *Arthur et al.* [1976]. We compute the eigenvalues/vectors from the real part of the average power spectral matrix. Then, using the eigenvectors, the averaged power spectral matrix is rotated into the principle axis coordinate system. The 2×2 submatrix in the plane defined by the intermediate and maximum eigenvectors is used to compute the ellipticity and the degree of polarization [e.g., *Fowler et al.*, 1967]. The computed ellipticity ranges from −1 (left-handed circular) to 0 (linear) and to 1 (right-handed circular), negative (positive) values indicating rotation in the left (right)-handed sense with respect to the IMF direction. The degree of polarization (DOP) which measures how coherent the waves are in the plane normal to the minimum variance direction varies from 0 (not coherent) to 1 (100% coherent). The white noise level of the DOP depends upon the type of averaging used to form the averaged power spectral matrix. Using simulated white noise as input into our polarization analysis code, we determined that the white noise level of the DOP is 0.41 ± 0.14 for the spectral matrix averaging used.

The wave vector direction is taken to be in the minimum variance direction. Because MESSENGER does not have an electric field instrument, the sign of the wave vector direction cannot be determined. The wave normal angle (WNA) is the angle between k and the IMF. Because of the sign ambiguity of the WNA, its values

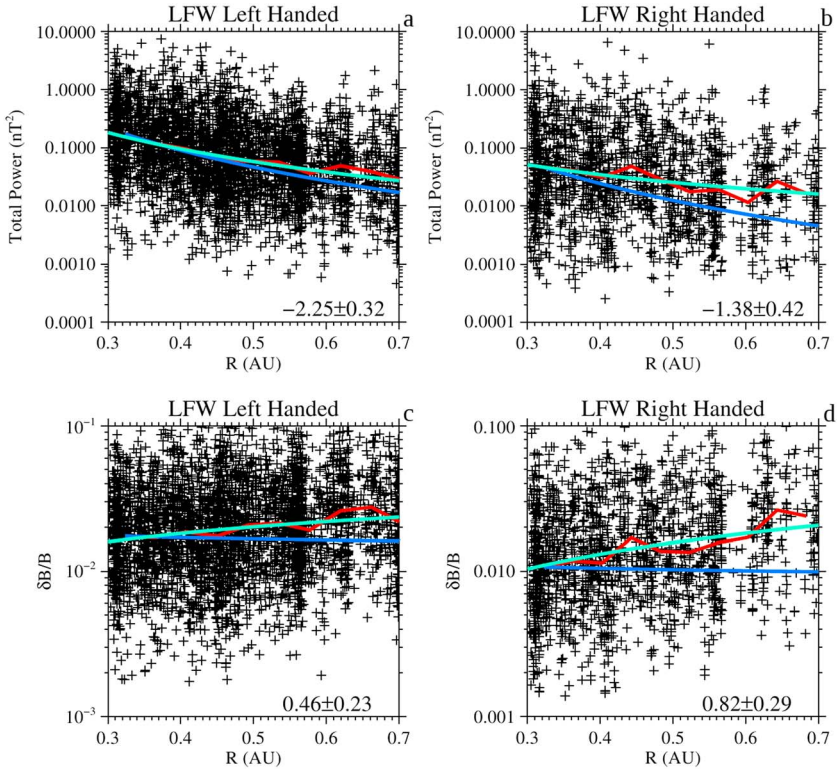

Figure 6. Scatterplot of total power versus R for (a) left-handed and (b) right-handed storms. Scatterplot of $\delta B/B$ versus R for (c) left-handed and (d) right-handed storms. The red curves are the running median. The cyan curves are power law fits to the observations, the exponent and its uncertainty are given in the lower right corner of each panel. The blue curves vary as R^{-3} in Figures 6a and 6b, and as $R^{-0.1}$ in Figures 6c and 6d.

are mapped to the first quadrant (0 to 90°). As discussed in the next section we need to resolve the sign of k in order to compute the Doppler shift between the spacecraft and solar wind frame, this is achieved by assuming that the waves are left handed in the solar wind frame of reference [*Jian et al.*, 2009, 2010, 2014]. Figures 2a and 3a show example spectrograms of ICW storms using these parameters.

Our computed spectrograms, such as those shown in Figures 2a and 3a, are composed of pixels of size 0.005 Hz by 0.25 s. Each pixel was assigned a value of 1 if its |ellipticity| > 0.65, the WNA < 40°, DOP > 0.7, and $f > 0.02$ Hz. All other pixels were assigned a value of 0. We applied "blob coloring" to the image composed of pixels of 1s and 0s. In blob coloring, each set of contiguous pixels with a value of 1 is assigned to the same blob. To remove background, blobs composed of less than 100 pixels were discarded; we note that this rejection criterion is arbitrary and was based on trial and error. An automated process was developed that scanned the 4 years of MESSENGER cruise phase data shown in Figure 1 for LFW events. Daily plots like those shown in Figures 2a and 2b were visually examined as a check of the automated selection of ICW events. Figures 2b and 3b show LFW events selected from blob analysis of the wave data shown in Figures 2a and 3a.

From the individual frequency-time measurements that compose the events, the median of the ratio of the intermediate to minimum and maximum to minimum eigenvalues are 20.7 and 29.4, respectively. These large ratios, coupled with the clustering of the ellipticities around ±0.8 (nearly circularly polarized), suggest that the wave normal angle is well defined and that the waves are fairly planar. From the eigenvalues, we estimate the uncertainty in minimum variance direction to be in the range ±5.9° [*Khrabrov and Sonnerup*, 1998].

Using the above criteria, 12,197 blobs of LFWs were identified. Histograms of some blob parameters are shown in Figure 4. As mentioned above, the cutoff of the minimum number of 100 pixels to define a blob is arbitrary and the number of occurrences of the blobs continues to climb as the number of pixels decrease as shown in Figure 4a. However, the temporal duration of the blobs (Figure 4b) does have a well-defined peak just below 10 min. The ellipticity (Figure 4c) has well-defined peaks around −0.8 or +0.8. The event

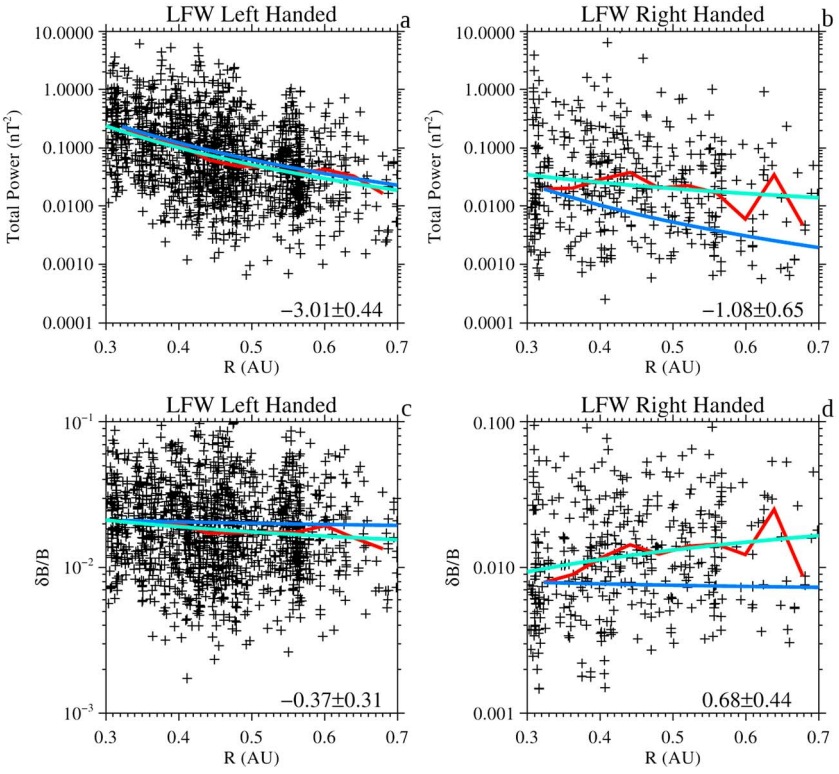

Figure 7. Formatted that same as Figure 6 but restricted to only LFW storms whose center frequency in the solar wind frame of reference lies within the range of 0.1 ± 0.02 Hz. Left and right handed refer to the polarization of the waves in the spacecraft frame of reference.

number of absolute ellipticity below 0.7 is very small; therefore, the statistics and occurrence rate (addressed later) will not change much if we change the |ellipticity| criterion from > 0.65 to > 0.7, which was used in *Jian et al*. [2009, 2010, 2014]. The wave normal angle (Figure 4d) has a well-defined peak around 7°. The angle between the IMF direction and the radial direction (φ_{BR}) has peaks (Figure 4e) around 20° and 160°. These values are close to the Parker spiral angles for a solar wind speed of 400 km/s at 0.3 AU, so it is important to normalize them by coverage. Figure 4f shows φ_{BR} normalized by coverage. The normalized probability peaks in the 0–10° and 170–180° bins, consistent with the findings of previous studies [e.g., *Jian et al*., 2009, 2010, 2014].

To Doppler shift the wave observations from the spacecraft frame to the solar wind frame, we need solar wind velocity and density. The MESSENGER Fast Imaging Plasma Spectrometer (FIPS) instrument [*Andrews et al*., 2007] has estimated solar wind speeds [*Gershman et al*., 2012] for only a very small fraction of the storms (see Figure 1e). FIPS can typically detect the solar wind near perihelion, when the aberration is large enough for FIPS to detect a portion of the solar wind ions. When FIPS sees the solar wind, it can sometimes estimate the speed, but it is not able to accurately estimate the density [*Gershman et al*., 2012]. Therefore, for periods when FIPS could not detect the solar wind, the average solar wind density and speed values at 1 AU are used, and the density values are scaled by R^{-2}. For events in which FIPS derived solar wind speed is available, we estimate the solar wind density (corrected by R^{-2}) from its speed using a relationship between the running medians of the density versus velocity, derived from the OMNI data during this 4 year time period, shown in Figure 5a. The 0.16th and 0.84th percentile curves (Figure 5a) give one an idea of the errors in density assignment.

3. Observations

Following *Jian et al*. [2014], an LFW event (one blob) whose duration is longer than 10 min is defined as a LFW storm. Of our 12,197 LFW events, 5506 of them are LFW storms, of which 1768 were right handed. The rest of this paper is focused on these storms. Figure 5b is the ratio of the left hand to total storms. This ratio is around

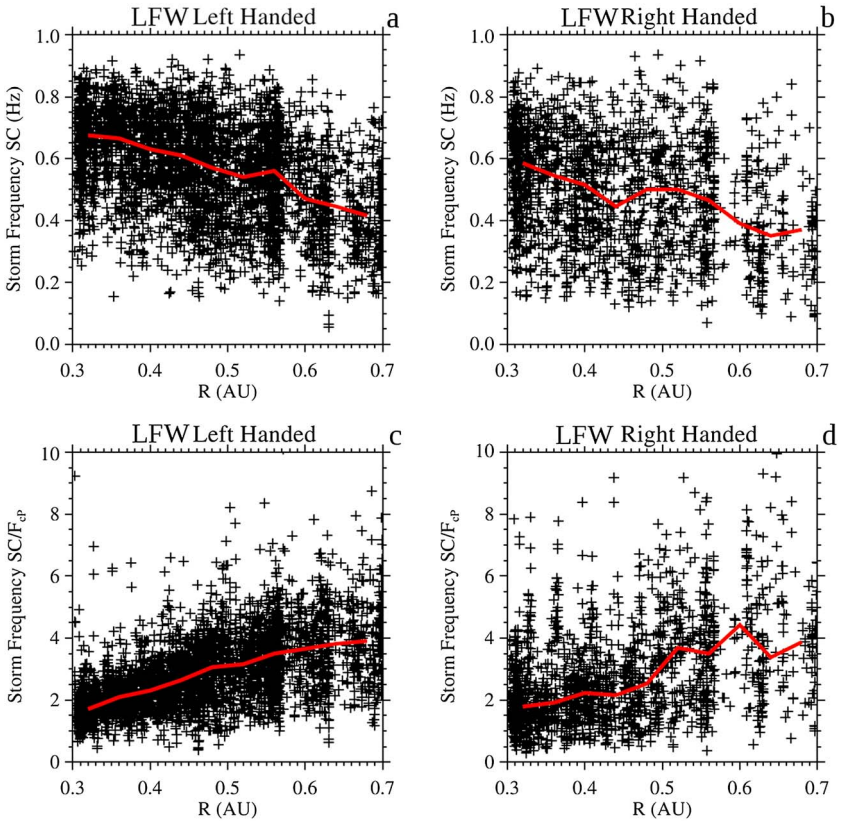

Figure 8. Scatterplot of LFW storm frequency in the spacecraft frame for (a) left-handed and (b) right-handed blobs and normalized by the proton cyclotron frequency for (c) left-handed and (d) right-handed blobs.

0.7, again consistent with *Jian et al*. [2010]. It slightly increases with increasing radial distance. The occurrence percentage of the LFW storms normalized by data coverage (when MESSENGER was sampling at $2\,s^{-1}$ or greater) is shown in Figure 5c. The percent occurrence is around 4 (2)% for the left-hand (right-hand) storm events. Using the observed φ_{BR} from the coverage and the occurrence probability curves as a function of φ_{BR} (Figure 4f), we predict the occurrence probability versus r for the coverage in Figure 5d. We computed the curves in Figure 5d by assigning a probability, using the curves in Figure 4f, to each measurement of φ_{BR} in a given radial bin, and computing the mean of those probabilities in each bin. In this section we present the observations with minimal discussion, saving the discussion for section 4.

A scatterplot of the total power in the units of nT^2 versus radial distance is shown in Figures 6a and 6b for left- and right-handed storms, respectively, in the spacecraft frame of reference. The total power is computed by the sum over all the pixels composing a storm of the power spectral density times the bandwidth (0.005 Hz). Because adjacent spectra (computed over 200 s) are staggered by 25 s, we have to include a correction factor to prevent overcounting of the power spectral density when computing to the total power. The normalized wave amplitude $\delta B/B$ versus radial distance is shown in Figures 6c and 6d for left- and right-handed storms, respectively. The red line in Figures 6a–6d is the running median, while the cyan line is the power law fit of the measurements with base R. The exponent and its uncertainty are given in the lower right corner of each panel. For the majority left-handed storms the exponent is -2.25 ± 0.32, we note that the running median (not shown) of the power spectral densities of individual pixels composing the storms also shows a $\sim R^{-2}$ dependence. The blue lines vary as R^{-3} for the total power and are based on a paper by *Hollweg* [1974], and $R^{-0.1}$ for $\delta B/B$. Figure 7 is similar to Figure 6 but restricted to frequencies in the solar wind frame between 0.1 ± 0.02 Hz and will be discussed in the next section. How the frequencies in the solar wind frame are estimated will be discussed next.

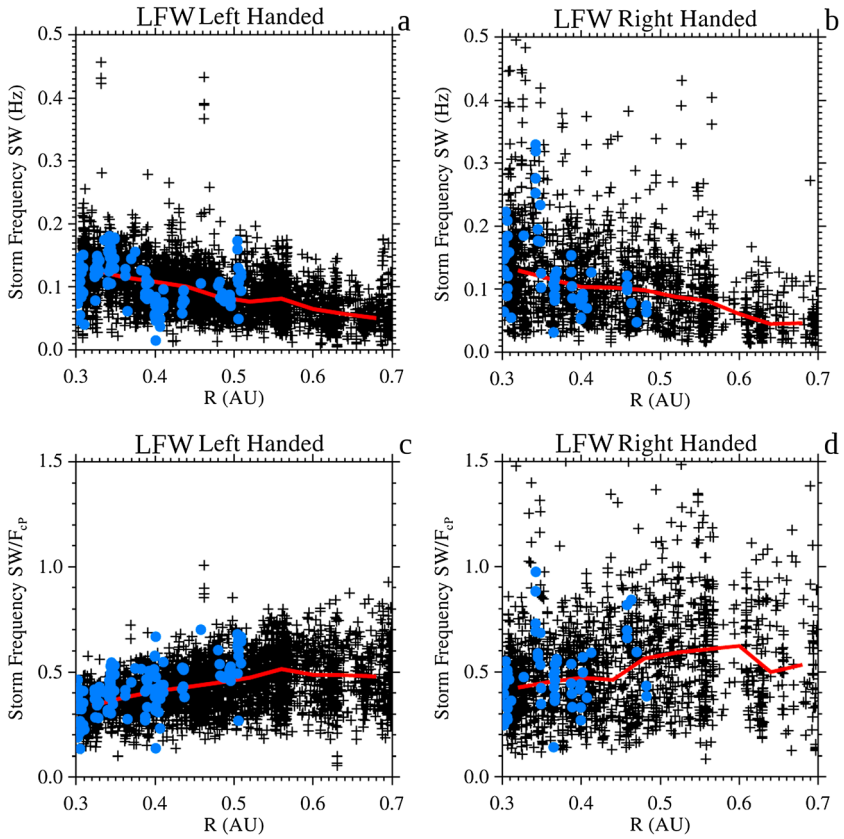

Figure 9. Scatterplot of LFW storm frequency in the solar wind frame for (a) left-handed and (b) right-handed blobs and normalized by the proton cyclotron frequency for (c) left-handed and (d) right-handed blobs. Since solar wind speed measurements by MESSENGER were only available for 153 of the 5506 storms, a solar wind density of 4.68 cm^{-3} and velocity of 384 km/s were used to compute the Doppler shift, see text for details. The blue dots are storms when FIPS solar wind measurements were used.

Scatterplots of frequency versus heliocentric radial distance in the spacecraft frame of reference are shown in Figures 8a and 8b for left- and right-handed LFW storms, respectively. The frequency of a storm is the median frequency of all individual frequency-time measurements that composed a storm. Scatterplots of frequency normalized by the local proton cyclotron frequency versus heliocentric radial distance in the spacecraft frame of reference are shown in Figures 8c and 8d for left- and right-handed storms, respectively. The red curves are running medians. Between 0.3 and 0.7 AU the median frequency drops from 0.65 to 0.40 Hz for left-handed storms and 0.60 to 0.35 Hz for right-handed storms, while the median normalized frequency rises.

Because we assume that the waves are generated in the bulk plasma flow frame (solar wind frame), we need to estimate the wave frequency in this frame, and the Doppler shift between the spacecraft and solar wind frame is quite large for these low-frequency waves. Equation (1) given by *Jian et al.* [2010] was used to compute the frequency in the solar wind frame of reference.

$$f_{sw} = f_{sc} - \frac{\boldsymbol{k}\cdot\boldsymbol{V}_{sw}}{2\pi} = f_{sc}/\left(1 + \frac{V_{sw}}{V_A}\hat{\boldsymbol{k}}\cdot\hat{\boldsymbol{V}}_{sw}\right), \quad (1)$$

where f_{SW} (f_{SC}) is the frequency in the solar wind (spacecraft) frame of reference and $\boldsymbol{k}\cdot\boldsymbol{V}_{SW}$ is the angular frequency of the Doppler shift. V_{SW} is the solar wind speed, and V_A is the Alfvén speed, V_A is used as a proxy for the phase velocity. As mentioned, MESSENGER does not measure the wave electric field, which is needed to resolve the sign ambiguity of k. To resolve the sign ambiguity, we follow the approach by *Jian et al.* [2009, 2010, 2014] where the waves are assumed to be left handed (ion cyclotron waves) in the solar wind frame of reference. For this data set $\left|\frac{V_{SW}}{V_A}\hat{k}\cdot\hat{V}_{SW}\right|$ tends to be always greater than 1, with a median value of 5.5, and greater than 2.0 for 99% of the measurements. If $\boldsymbol{k}\cdot\boldsymbol{V}_{SW} > 0$, then the sign of the denominator in equation

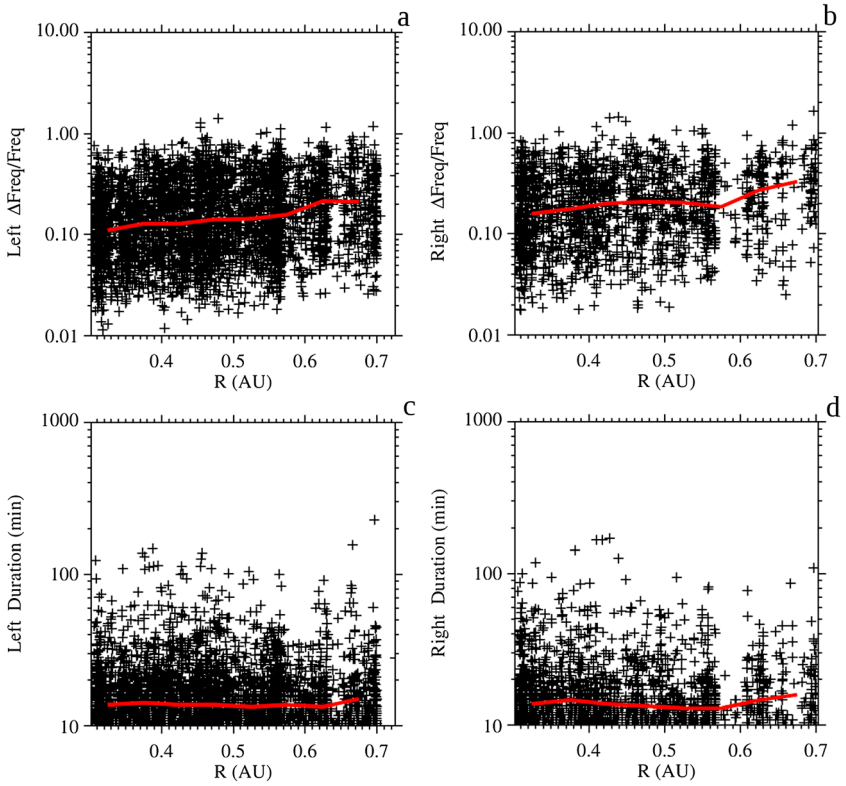

Figure 10. The width in frequency divided by the median frequency of each storm versus R is plotted for (a) left-handed storms and (b) right-handed storms. The duration of the storms in minutes plotted for (c) left-handed storms and (d) right-handed storms. The red line is the running median.

(1) is positive and the waves will be left handed in the spacecraft frame. If $\boldsymbol{k} \cdot \boldsymbol{V}_{SW} < 0$, then the sign of the denominator in equation (1) is negative and the waves will be right handed in the spacecraft frame. As noted, when solar wind speed measurements by the FIPS instrument are not available, to compute V_A we used the average solar wind density (4.68 cm^{-3} and scaled by R^{-2}) and speed (384 km/s) at 1 AU derived from the OMNI data over the same time period of this study.

Figure 9 is a scatterplot of storm frequency versus heliocentric radial distance in the solar wind frame of reference. Figures 8a and 8c are storms that are left handed in this frame. Figures 8b and 8c are storms that are right handed in this frame. Figures 8c and 8d are normalized by the local proton cyclotron frequency. The red curve in Figures 8a–8d is the running median. The observed storm frequency decreases with increasing radial distance for both left- and right-handed storms, while the observed normalized frequency increases with increasing radial distance. Using the observed solar wind velocity and pseudodensity for the handful of storms, we observed the same trends, shown as blue dots in Figure 9.

Figures 10a and 10b are plots of the frequency bandwidth of the storms divided by the median storm frequency for left- and right-handed storms, respectively. There is a small increase in the normalized frequency bandwidth versus R. This is consistent with the increased spread of f_{SC}/f_{cP} and f_{SW}/f_{cP} with R in Figures 8 and 9 of this study and in Figure 15 of *Jian et al*. [2014]. This is possibly due to the energy dissipation from waves to solar wind ions. Figures 10c and 10d are plots of the time duration of the storms for left- and right-handed storms, respectively. The running median of the time duration is relatively flat.

4. Discussion and Conclusion

Right-handed and left-handed storms tend to occur in separate clusters. Occasionally, the LFW storms of opposite polarization in spacecraft frame are observed simultaneously (e.g., Figure 2) or close together but separated in time (e.g., Figure 3). Out of 1768 right-handed storms, 204 (11.5%) overlapped with left-handed storms in time, and 168 (9.5%) occurred within 1 h of a left-handed storm. In total, the nearby occurrence of both

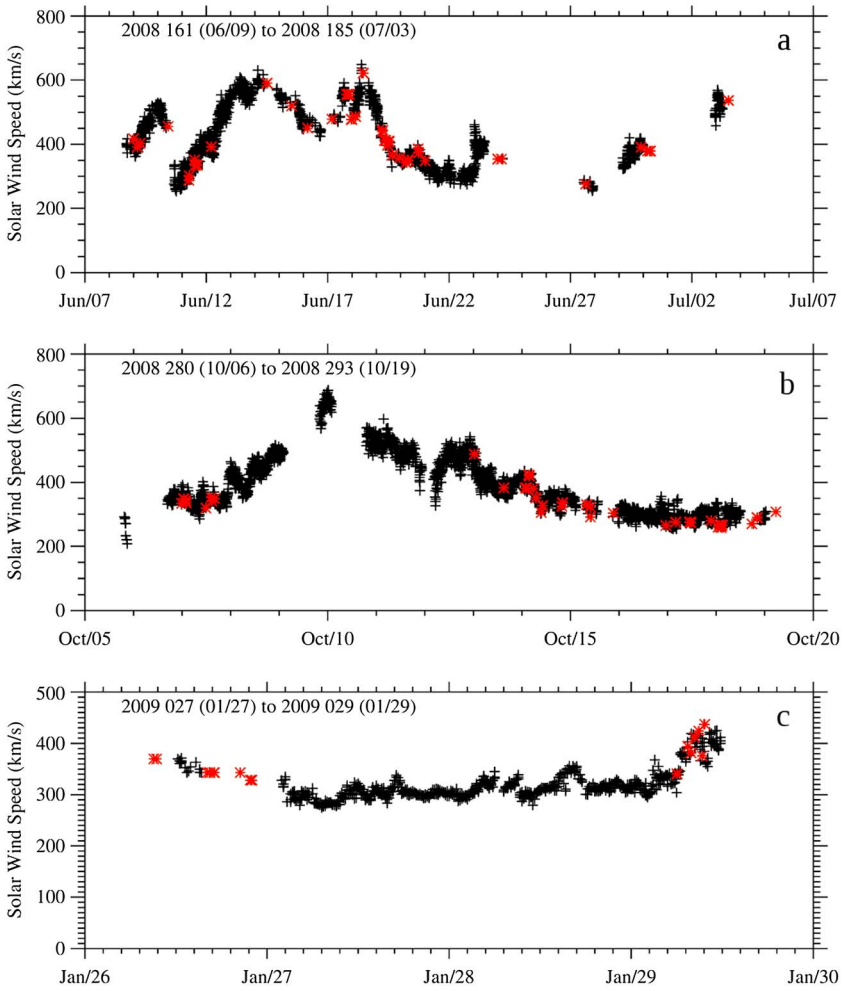

Figure 11. The periods when MESSENGER FIPS solar wind measurements are available: the time spans are (a) 31 days, (b) 16 days, and (c) 5 days. The red dots indicate when LFW storms were occurring within 24 h of a measurement. Not enough solar wind measurements are available to reach the conclusion by *Jian et al.* [2014], Figure 11b is highly suggestive.

polarizations is observed 21% of the time for all right-handed storms, and 10% for all left-handed storms, consistent with 13% for right-handed storms and 11% for left-handed storms at 1 AU [*Jian et al.*, 2014]. Among the 204 concurrent events, in 191 the left-handed frequency was greater than the right-handed frequency (for example, Figure 2) with a median overlap time of 12 min, and in 13 the right-handed frequency was greater than the left-handed frequency with a median overlap time of 5 min. If the left-handed and right-handed waves originate from the same source region and the opposite polarization is due to outward/inward propagation, then from equation (1), the left-handed waves would have higher f_{SC} than right-handed ones. This is probably why in concurrent events we see higher f_{SC} for left-handed waves much more frequently.

Looking at Figures 6–9, using the median curves, we estimate the following parameters at 0.3 AU, total wave power of ~0.2 nT^2, $\delta B/B$ of ~0.02, f_{SC} of ~0.65 Hz, f_{SC}/f_{cP} of 1.6, f_{SW} of ~0.14 Hz, and f_{SW}/f_{cP} of ~0.35. Compared to values from *Jian et al.* [2010] of total wave power of ~0.53 nT^2, $\delta B/B$ of ~0.03, f_{SC} of ~0.59 Hz, f_{SC}/f_{cP} of 1.4, f_{SW} of ~0.14 Hz, and f_{SW}/f_{cP} of ~0.35, the results are consistent, except the total power in their study is 2.5 times larger than that of our study, and $\delta B/B$ is slightly larger in their study. One possible reason is that the event selection is automated in this study instead of tedious manual selection used in *Jian et al.* [2010]. For manual event selection, more powerful events are probably more readily identified than the weaker events. This is also borne out by occurrence rates that are a factor of 6 larger in this study compared to previous studies. The occurrence at 0.3 AU is ~4% for left-handed and ~2% for right-handed emissions compared to ~1% for total from *Jian et al.* [2010].

Table 1. Power Law Fits to the Power and $\delta B/B$ as a Function of Heliocentric Distance R, for Different Frequency Bins in the Solar Wind Frame of Reference[a]

SW Frame	Left-Handed Storms			Right-Handed Storms		
Frequency (Hz)	#	a	b	#	a	b
0.08 ± 0.01	721	−3.28 ± 0.51	−0.53 ± 0.36	234	−0.86 ± 0.73	0.73 ± 0.50
0.08 ± 0.02	1374	−3.02 ± 0.44	−0.36 ± 0.31	472	−0.55 ± 0.61	0.87 ± 0.41
0.10 ± 0.01	726	−2.70 ± 0.52	−0.28 ± 0.36	202	−0.71 ± 0.76	0.79 ± 0.52
0.10 ± 0.02	1392	−3.01 ± 0.44	−0.37 ± 0.31	400	−1.08 ± 0.65	0.68 ± 0.44
0.12 ± 0.01	558	−3.54 ± 0.57	−0.72 ± 0.39	182	−1.52 ± 0.75	0.48 ± 0.51
0.12 ± 0.02	1142	−3.23 ± 0.47	−0.50 ± 0.32	360	−1.68 ± 0.66	0.39 ± 0.45
0.14 ± 0.01	334	−3.20 ± 0.66	−0.55 ± 0.46	129	−1.91 ± 0.89	0.17 ± 0.61
0.14 ± 0.02	689	−3.24 ± 0.53	−0.55 ± 0.36	307	−1.74 ± 0.70	0.35 ± 0.48

[a]Divided into left- and right-handed storms in the spacecraft frame of reference. The power $\sim R^a$ and $\delta B/B \sim R^b$, where a and b are the power law coefficients, and # is the number of storms in a frequency bin.

For the more dominant left-handed mode, no clear radial dependence is observed in the occurrence in Figure 5c. At first this seems puzzling, since on average the IMF direction should follow the Parker spiral. For a solar wind speed of 430 km/s, the Parker spiral angle is 17° at 0.3 AU, 36° at 0.7 AU, and 46° at 1 AU. Looking at Figure 4f, for the left-hand mode, the occurrence is ~13% at 0.3 AU, ~4% at 0.7 AU, and ~1% at 1.0 AU for the Parker spiral angle given above, which is clearly not observed in Figure 5c. We believe this discrepancy is because for a given radial distance and solar wind velocity, the scatter of φ_{BR} about the Parker spiral is large. We used the occurrence curves in figure 4f to predict the mean occurrence versus radial distance from the φ_{BR} measurements made during the period of this study. Note that the dependence is slowly decreasing with radius but not at the large rate predicted from the Parker spiral. Figure 5d shows that the change (0.25%) in predicted drop off rate is much smaller between 0.3 and 0.7 AU than if one used the Parker spiral. Even though the occurrence is a factor of 6 larger than the studies of *Jian et al*. [2010, 2014], the trend in the radial variation is consistent with *Jian et al*. [2010] at 0.3 AU and *Jian et al*. [2014] at 1 AU, where the occurrence was nearly the same around 1% at both radial distances.

The differences in occurrence versus radial distance between Figures 5c and 5d could be because additional parameters along with φ_{BR} must be important in the generation of these waves. One parameter identified by *Jian et al*. [2014] is rarefaction regions that follow high-speed streams. They hypothesized that in these regions the bulk ion anisotropies are larger and ion beams occur more often; and therefore, these regions are more likely to be unstable to the generation of LFWs. Do we see this for the three periods where we have solar wind speed coverage shown in Figure 1e? Figure 11 is a plot of the solar wind speed for these three intervals, the middle interval clearly follows a high-speed stream, consistent with their findings from STEREO. We need more intervals of solar wind speed from FIPS to reach any definitive conclusions. Looking at Figure 1 there are seven more near perihelion intervals where FIPS potentially could detect the solar wind that have not been analyzed for solar wind speed. Measurements of the differential flow speed and ion perpendicular-to-parallel temperature ratios are needed in conjunction with the storm observations, currently we are conducting such studies using the Wind spacecraft data.

Figure 5b shows a slight increase in the ratio of left to total storms with increasing radial distance. Note that *Jian et al*. [2014] observe the opposite, comparing observations at 0.3 and 1 AU, they found a percentage of 72% at 0.3 AU and 55% at 1 AU. If the mechanism in *Podesta and Gary* [2011b] is the reason why LFWs occur more frequently, then the ratio of left- to right-handed waves should approach unity as $|V_{He++} - V_{H+}|$ approaches 0. Figure 11 of *Marsch et al*. [1982] shows that the differential flow decreases with increasing radial distance, which also implies that the ratio of left- to right-handed waves should approach unity as the radial distance increases. This is consistent with *Jian et al*. [2014], but not with that of Figure 5b, but our study only goes out to 0.7 AU.

Studies of the dependence with heliocentric distance of the observed wave amplitude and power of Alfvénic turbulence show that this dependence agrees [e.g., *Roberts et al*., 1990] with the radial dependence predicted from propagation of waves from a source region which is assumed to be near the Sun [e.g., *Hollweg*, 1974]. In his derivation, *Hollweg* [1974] assumed energy conservation and that the Wentzel-Kramers-Brillouin (WKB) approximation holds from which he predicted how $< \delta B^2 >$ of a transverse Alfvén wave will change as the

wave propagates in the solar wind, equation (23) of *Hollweg* [1974] predicts that the variation of $<\delta B^2> \propto \rho^{3/2}$, where ρ is the solar wind mass density. As the solar wind propagates outward, taking $\rho \propto \sim R^{-2}$ [e.g., *Köhnlein* [1996]], one predicts that $<\delta B^2> \propto R^{-3}$. Since the wave magnetic field fluctuations of these LFW storms are transverse to the background field ***B***, we assume, if they are generated inside of 0.3 AU, that they will show a similar R^{-3} radial dependence of the power if the dissipation is small. Because frequency is conserved in the application of the WKB approximation, in making radial comparisons we restrict the frequencies in Figure 7 to 0.1 ± 0.02 Hz in the solar wind frame of reference. The observed LFW power varies as $R^{-3.01 \pm 0.44}$ and $R^{-1.08 \pm 0.65}$ for left-handed (Figure 7a) and right-handed (Figure 7b) LFW storms, respectively, so to within the error bars the decrease in power with radial distance is consistent with the predication of *Hollweg* [1974] for left-handed LFW storms and not consistent for right-handed LFW storms. From a power law fit of B during over all of these storms, we get $B \propto R^{-1.4}$, so one predicts $\delta B/B \propto R^{-0.1}$. The observed $\delta B/B$ varies as $R^{-0.37 \pm 0.31}$ and $R^{0.68 \pm 0.44}$ for left-handed (Figure 7c) and right-handed (Figure 7d) LFW storms, respectively. To just within the error bars, the decrease in $\delta B/B$ with R is consistent with the predication of *Hollweg* [1974] for left-handed storms and not consistent for right-handed storms. Table 1 shows power law fits to δB^2 and $\delta B/B$ for different center frequencies and frequency bin sizes in the solar wind frame for both left- and right-handed LFW storms. For the left-handed LFW storms, δB^2 and $\delta B/B$ are consistent with a source near the Sun, and for right-handed storms it is not.

Based on comparisons with *Hollweg* [1974], this study suggests that a large fraction of the left-handed LFW storms are generated close to the Sun, while the right-handed LFW storms are not. Modeling of these LFWs in a realistic expanding solar wind will help explain some of our findings.

Acknowledgments
The MESSENGER data used in this study were obtained from the Planetary Data System at http://pds.nasa.gov/. The OMNI data were obtained from the GSFC/SPDF OMNIWeb interface at http://omniweb.gsfc.nasa.gov. This work is supported by NASA research grants NNX13AI65G and NNX15AB75G.

References

Anderson, B. J., M. H. Acuña, D. A. Lohr, J. Scheifele, A. Raval, H. Korth, and J. A. Slavin (2007), The Magnetometer instrument on MESSENGER, *Space Sci. Rev.*, *131*, 417–450, doi:10.1007/s11214-007-9246-7.

Andrews, G. B., et al. (2007), The Energetic Particle and Plasma Spectrometer instrument on the MESSENGER spacecraft, *Space Sci. Rev.*, *131*, 523–556.

Arthur, C. W., R. L. McPherron, and J. D. Means (1976), A comparative study of three techniques for using the spectral matrix in wave analysis, *Radio Sci.*, *11*(10), 833–845, doi:10.1029/RS011i010p00833.

Fowler, R. A., B. J. Kotick, and R. D. Elliot (1967), Polarization analysis of natural and artificially induced geomagnetic micropulsations, *J. Geophys. Res.*, *72*, 2871–2883, doi:10.1029/JZ072i011p02871.

Gary, S. P., L. Yin, D. Winske, L. Ofman, B. E. Goldstein, and M. Neugebauer (2003), Consequences of proton and alpha anisotropies in the solar wind: Hybrid simulations, *J. Geophys. Res.*, *108*(A2), 1068, doi:10.1029/2002JA009654.

Gershman, D. J., T. H. Zurbuchen, L. A. Fisk, J. A. Gilbert, J. M. Raines, B. J. Anderson, C. W. Smith, H. Korth, and S. C. Solomon (2012), Solar wind alpha particles and heavy ions in the inner heliosphere observed with MESSENGER, *J. Geophys. Res.*, *117*, A00M02, doi:10.1029/2012JA017829.

Gershman, D. J., G. Gloeckler, J. A. Gilbert, J. M. Raines, L. A. Fisk, S. C. Solomon, E. C. Stone, and T. H. Zurbuchen (2013), Observations of interstellar helium pickup ions in the inner heliosphere, *J. Geophys. Res. Space Physics*, *118*, 1389–1402, doi:10.1002/jgra.50227.

He, J., E. Marsch, C. Tu, S. Yao, and H. Tian (2011), Possible evidence of Alfvén-cyclotron waves in the angle distribution of magnetic helicity of solar wind turbulence, *Astrophys. J.*, *731*, 85.

Hollweg, J. V. (1974), Transverse Alfvén waves in the solar wind: Arbitrary **k**, **v** 0, **B** 0, and $|\delta \mathbf{B}|$, *J. Geophys. Res.*, *79*(10), 1539–1541, doi:10.1029/JA079i010p01539.

Jian, L. K., C. T. Russell, J. G. Luhmann, R. J. Strangeway, J. S. Leisner, and A. B. Galvin (2009), Ion cyclotron waves in the solar wind observed by STEREO near 1 AU, *Astrophys. J.*, *701*, L105, doi:10.1088/0004-637X/701/2/L105.

Jian, L. K., C. T. Russell, J. G. Luhmann, B. J. Anderson, S. A. Boardsen, R. J. Strangeway, M. M. Cowee, and A. Wennmacher (2010), Observations of ion cyclotron waves in the solar wind near 0.3 AU, *J. Geophys. Res.*, *115*, A12115, doi:10.1029/2010JA015737.

Jian, L. K., H. Y. Wei, C. T. Russell, J. G. Luhmann, B. Klecker, N. Omidi, P. A. Isenberg, M. L. Goldstein, A. Figueroa-Vinas, and X. Blanco-Cano (2014), Electromagnetic waves near the proton cyclotron frequency: STEREO observations, *Astrophys. J.*, *786*, L123, doi:10.1088/0004-637X/786/2/123.

Kasper, J. C., A. J. Lazarus, and S. P. Gary (2008), Hot solar-wind helium: Direct evidence for local heating by Alfvén-cyclotron dissipation, *Phys. Rev. Lett.*, *101*(26), doi:10.1103/PhysRevLett.101.261103.

Khrabrov, A. V., and B. U. Sonnerup (1998), Error estimates for minimum variance analysis, *J. Geophys. Res.*, *103*(A4), 6641–6651, doi:10.1029/97JA03731.

Köhnlein, W. (1996), Radial dependence of solar wind parameters in the ecliptic (1.1 $R_\odot$–61 AU), *Sol. Phys.*, *169*(1), doi:10.1007/BF00153841.

Marsch, E., K.-H. Mühlhäuser, H. Rosenbauer, R. Schwenn, and F. M. Neubauer (1982), Solar wind helium ions: Observations of the Helios solar probes between 0.3 and 1 AU, *J. Geophys. Res.*, *87*(A1), 35–51, doi:10.1029/JA087iA01p00035.

Murphy, N., E. J. Smith, B. T. Tsurutani, A. Balogh, and D. J. Southwood (1995), Further studies of waves accompanying the solar wind pick-up of interstellar hydrogen, *Space Sci. Rev.*, *72*(1–2), doi:10.1007/BF00768819.

Ofman, L., A. Viñas, and S. P. Gary (2001), Constraints on the O^{+5} anisotropy in the solar corona, *Astrophys. J.*, *547*, L175.

Ofman, L., S. P. Gary, and A. Viñas (2002), Resonant heating and acceleration of ions in coronal holes driven by cyclotron resonant spectra, *J. Geophys. Res.*, *107*(A12), 1461, doi:10.1029/2002JA009432.

Omidi, N., P. Isenberg, C. T. Russell, L. K. Jian, and H. Y. Wei (2014a), Generation of ion cyclotron waves in the corona and solar wind, *J. Geophys. Res. Space Physics*, *119*, 1442–1454, doi:10.1002/2013JA019474.

Omidi, N., C. T. Russell, L. K. Jian, P. Isenberg, and H. Y. Wei (2014b), Generation and propagation of ion cyclotron waves in nonuniform magnetic field: Application to the corona and solar wind, *J. Geophys. Res. Space Physics*, *119*, 8750–8763, doi:10.1002/2014JA020315.

Podesta, J. J., and S. P. Gary (2011a), Magnetic helicity spectrum of solar wind fluctuations as a function of the angle with respect to the local mean magnetic field, *Astrophys. J.*, *734*, 15.

Podesta, J. J., and S. P. Gary (2011b), Effect of differential flow of alpha particles on proton pressure anisotropy instabilities in the solar wind, *Astrophys. J.*, *742*, 41, doi:10.1088/0004-637X/742/1/41.

Roberts, D. A., M. L. Goldstein, and L. W. Klein (1990), The amplitudes of interplanetary fluctuations: Stream structure, heliocentric distance, and frequency dependence, *J. Geophys. Res.*, *95*(A4), 4203–4216, doi:10.1029/JA095iA04p04203.

Steinberg, J. T., A. J. Lazarus, K. W. Ogilvie, R. Lepping, and J. Byrnes (1996), Differential flow between solar wind protons and alpha particles: First WIND observations, *Geophys. Res. Lett.*, *23*(10), 1183–1186, doi:10.1029/96GL00628.

Tsurutani, B. T., J. K. Arballo, J. Mok, E. J. Smith, G. M. Mason, and L. C. Tan (1994), Electromagnetic waves with frequencies near the local proton gyrofrequency: ISEE-3 1 AU observations, *Geophys. Res. Lett.*, *21*, 633–636, doi:10.1029/94GL00566.